

# The use of the NEXTGEN model atmospheres for cool giants in a light curve synthesis code

J.A. Orosz<sup>1</sup> and P.H. Hauschildt<sup>2</sup>

<sup>1</sup> Utrecht University, Astronomical Institute, P.O. Box 80000, 3508 TA Utrecht, The Netherlands (J.A.Orosz@astro.uu.nl)

<sup>2</sup> The University of Georgia, Department of Physics & Astronomy and Center for Simulational Physics, Athens, GA 30602-2451, USA (yeti@hobbes.physast.uga.edu)

Received 3 May 2000 / Accepted 29 September 2000

**Abstract.** We have written a light curve synthesis code that makes direct use of model atmosphere specific intensities, in particular the NEXTGEN model atmosphere grid for cool giants ( $T_{\text{eff}} \leq 6800$  K and  $\log(g) \leq 3.5$ , Hauschildt et al. 1999). We point out that these models (computed using spherical geometry) predict a limb darkening behaviour that deviates significantly from a simple linear or two-parameter law (there is less intensity at the limb of the star). The presence of a significantly nonlinear limb darkening law has two main consequences. First, the ellipsoidal light curve computed for a tidally distorted giant using the NEXTGEN intensities is in general different from the light curve computed using the same geometry but with the black body approximation and a one- or two-parameter limb darkening law. In most cases the light curves computed with the NEXTGEN intensities have deeper minima than their black body counterparts. Thus the light curve solutions for binaries with a giant component obtained with models with near linear limb darkening (either black body or plane-parallel model atmosphere intensities) are biased. Observations over a wide wavelength range (i.e. both the optical and infrared) are particularly useful in discriminating between models with nearly linear limb darkening and the NEXTGEN models. Second, we show that rotational broadening kernels for Roche lobe filling (or nearly filling) giants can be significantly different from analytic kernels due to a combination of the nonspherical shape of the star and the radical departure from a simple limb darkening law. As a result, geometrical information inferred from  $V_{\text{rot}} \sin i$  measurements of cool giants in binary systems are likewise biased.

**Key words:** methods: miscellaneous – stars: atmospheres – stars: binaries: close

## 1. Introduction

The study of close binary stars is of interest for several reasons. For example, the understanding the structure and evolution of stars is a basic goal of stellar astronomy, and is required in most other branches of astronomy. Critical tests of evolution theory

(i.e. predicting the radius and luminosity of a star as a function of its mass and age) for stars other than the Sun are practical only for a small set of eclipsing binary stars (see, e.g., Pols et al. 1997; Schröder et al. 1997; Lacy et al. 2000). In addition, our knowledge of the masses of stellar black holes (and many neutron stars and white dwarfs as well) depends on our ability to interpret ellipsoidal and usually non-eclipsing light curves (e.g. Avni & Bahcall 1975; Avni 1978; McClintock & Remillard 1990; Haswell et al. 1993; Shahbaz et al. 1994; Sanwal et al. 1996; Orosz & Bailyn 1997). Finally, considerable observational effort has been put forth recently to use detached eclipsing binaries as extragalactic distance indicators (Mochejska et al. 1998; Ribas et al. 2000). Since close binary stars are of such importance, it is crucial that we have the ability to construct accurate synthetic light curves for a variety of close binaries.

The light curve expected from a particular close binary depends on the system geometry (i.e. the figures of the stars, their relative sizes, separation, viewing angle, etc.) and on the radiative properties of the stars, which are set mainly by their effective temperatures, surface gravities and chemical compositions. The equations describing the basic system geometry for a close binary are reasonably simple and have been known for a long time (e.g. see the text by Kopal 1959). In practice, however, the direct computation of light curves requires a computer, and codes to compute light curves have been in use since the late 1960s (e.g. Lucy 1967; Hill & Hutchings 1970; Wilson & Devinney 1971; Mochnacki & Doughty 1972; Avni & Bahcall 1975; see also the review by Wilson 1994). On the other hand, the detailed computation of stellar atmosphere models which describe the specific intensity of radiation emitted by the stellar surfaces is quite involved. As a result, approximations are frequently used in the computations of light curves. The Planck function is usually used to compute the normal monochromatic intensity of a surface element with an effective temperature  $T_{\text{eff}}$ :

$$I_0 \propto [\exp(hc/k\lambda T_{\text{eff}}) - 1]^{-1} \quad (1)$$

where  $\lambda$  is the effective wavelength of the observation and  $h$ ,  $c$ , and  $k$  are the usual physical constants. After  $I_0$  is found, the specific intensities for other emergent angles are computed using a simple parameterisation (the “limb darkening law”):

$$I(\mu) = I_0[1 - x(1 - \mu)]. \quad (2)$$

The coefficient  $x$  depends on the temperature, gravity, and chemical composition of the star being modelled. There are also many two-parameter limb darkening laws including a “quadratic” law:

$$I(\mu) = I_0[1 - x(1 - \mu) - y(1 - \mu)^2], \quad (3)$$

the “square root” law (Díaz-Cordovés & Giménez 1992):

$$I(\mu) = I_0[1 - x(1 - \mu) - y(1 - \sqrt{\mu})], \quad (4)$$

or the “logarithmic” law (Klinglesmith & Sobieski 1970):

$$I(\mu) = I_0[1 - x(1 - \mu) - y\mu \ln \mu]. \quad (5)$$

There are many tabulations of the coefficients for these various laws for a wide variety of temperatures, gravities, and chemical compositions (e.g. Al-Naimiy 1978; Wade & Rucinski 1985; Van Hamme 1993; Claret 1998).

We discuss in this paper our technique for computing light curves using model atmosphere specific intensities directly, thereby eliminating the need for the black body approximation and the one- or two-parameter limb darkening laws. Although our emphasis here is on stars with low effective temperatures and surface gravities ( $T_{\text{eff}} \leq 6800$  K and  $\log g \leq 3.5$ ), the technique is quite general. In the next section we discuss some previous work in this area and give details of our method. We then discuss some of the basic results and their implications, and give a summary of this work. We have also included an appendix to the paper which gives some of the details of our light curve code not directly related to the stellar atmospheres.

## 2. Computational technique

### 2.1. Previous work

The use of model atmosphere computations inside a light curve synthesis code is by no means new. The widely used Wilson-Devinney (1971; hereafter W-D) code has routine which applies a correction to the normal (black body) intensity:

$$I_0^{\text{corr}} = I_0 r(T_{\text{eff}}, \log g, \lambda), \quad (6)$$

where  $r(T_{\text{eff}}, \log g, \lambda)$  is the ratio of the filter-integrated stellar atmosphere model characterised by  $T_{\text{eff}}$  and  $\log g$  to the filter-integrated blackbody intensity. The specific intensities for other angles are then computed from  $I_0^{\text{corr}}$  using the limb darkening law. The correction routine supplied with the W-D code is based on the Carbon & Gingerich (1969) models. R.E. Wilson (priv. comm. 2000) informs us he is in the process of updating the correction routine. Milone et al. (1992) have independently written a correction routine for the W-D code based on the Kurucz (1979) models. Linnell & Hubeny (1994, 1996) have written a series of codes to compute synthetic spectra and light curves for binary stars, including ones with disks. They use Hubeny’s general spectrum synthesis code SYNSPEC (Hubeny et al. 1994) to generate the model spectra, using as input Kurucz (1979) atmosphere models for cool stars ( $T_{\text{eff}} \leq 10000$  K) and TLUSTY (Hubeny 1988) and TLUSDISK (Hubeny 1991) models for hotter stars and disks, respectively. They have applied

their model with some success to  $\beta$  Lyrae (Linnell et al. 1998a) and MR Cygni (Linnell et al. 1998b). Tjemkes et al. (1986) have used Kurucz (1979) models in their light curve synthesis code by tabulating filter-integrated normal intensities for a grid of effective temperatures and surface gravities. Specific intensities for other emergent angles are computed from a limb darkening law tabulated from Kurucz models. This code has been applied successfully to X-ray binaries such as LMC X-4 (Heemskerk & van Paradijs 1989) and GRO J1655-40 (van der Hooft et al. 1998) and to the millisecond pulsar PSR 1957+20 (Callanan et al. 1995). Shahbaz et al. (1994) mention of the use of Kurucz (1979) fluxes in a code used at Oxford, but this paper does not specifically describe how the model atmosphere fluxes are incorporated into the light curve synthesis code. Similarly, Sanwal et al. (1996) mention the use of Bell & Gustafsson (1989) model atmosphere fluxes in the light-curve synthesis code developed at the University of Texas at Austin (Zhang et al. 1986; Haswell et al. 1993) without giving specific details.

### 2.2. Current work

We use a technique suggested to us by Marten van Kerkwijk to incorporate model atmosphere intensities into our light curve synthesis code. In general, a detailed model atmosphere computation yields the specific intensity  $I(\lambda, \mu)$  at a given wavelength  $\lambda$  and emergent angle  $\mu = \cos \theta$ , where  $\mu = 1$  at the centre of the apparent stellar disk and  $\mu = 0$  at the limb. The total disk-integrated intensity  $I(\lambda)$  observed at the wavelength  $\lambda$  is then

$$I(\lambda) = \int_0^1 I(\lambda, \mu) \mu d\mu. \quad (7)$$

Normally, the light curves of a binary star are observed in a broad bandpass. The observed intensity  $I_{\text{FILT}}$  in a given bandpass is

$$\begin{aligned} I_{\text{FILT}} &= \int_{-\infty}^{+\infty} I(\lambda) W_{\text{FILT}}(\lambda) d\lambda \\ &= \int_{-\infty}^{+\infty} \left[ \int_0^1 I(\lambda, \mu) \mu d\mu \right] W_{\text{FILT}}(\lambda) d\lambda, \end{aligned} \quad (8)$$

where  $W_{\text{FILT}}$  is the wavelength-dependent transmission of the filter bandpass in question. We can reverse the order of the integrals in Eq. (8) to give

$$\begin{aligned} I_{\text{FILT}} &= \int_0^1 \left[ \int_{-\infty}^{+\infty} I(\lambda, \mu) W_{\text{FILT}}(\lambda) d\lambda \right] \mu d\mu \\ &= \int_0^1 I_{\text{FILT}}(\mu) \mu d\mu. \end{aligned} \quad (9)$$

The quantity in square brackets in Eq. (9), namely

$$I_{\text{FILT}}(\mu) = \int_{-\infty}^{+\infty} I(\lambda, \mu) W_{\text{FILT}}(\lambda) d\lambda \quad (10)$$

is independent of any geometry (for non-irradiated atmospheres), and as such can be computed in advance of the light curve synthesis computations.

In our current implementation we compute for each model characterised by a temperature  $T_{\text{eff}}$  and gravity  $\log g$  a table of eight filter-integrated intensities for each specific angle  $\mu$ . The eight filters currently are the Johnson *UBVRIJHK* system where we have used the optical filter response curves given in Bessell (1990) and the infrared filter response curves given in Bessell & Brett (1988). Using all of the models we then generate a table of the form

---

```

T1 g1
Nmu
mu1 I(1,1) I(1,2) ... I(1,7) I(1,8)
mu2 I(2,1) I(2,2) ... I(2,7) I(2,8)
...
muN I(N,1) I(N,2) ... I(N,7) I(N,8)
T1 g2
Nmu
mu1 I(1,1) I(1,2) ... I(1,7) I(1,8)
mu2 I(2,1) I(2,2) ... I(2,7) I(2,8)
...
muN I(N,1) I(N,2) ... I(N,7) I(N,8)
T2 g1
...

```

---

The first two numbers are the temperature and gravity of the first model. The next line gives the number of specific intensities that follow. The next  $N_\mu$  lines give the value of  $\mu$  followed by the eight filter-integrated intensities. The format is then repeated for the additional models. The table is sorted in order of increasing temperature, and for each temperature, the table is sorted in order of increasing gravity.

During the course of computing a synthetic light curve the specific intensity of each surface element must be specified. These values of  $I(T_{\text{inp}}, \log g_{\text{inp}}, \mu_{\text{inp}})$  are interpolated from the table using a simple linear interpolation procedure. First, we locate the 4 nearest models  $(T_{\text{up}}, \log g_{\text{up}})$ ,  $(T_{\text{up}}, \log g_{\text{low}})$ ,  $(T_{\text{low}}, \log g_{\text{up}})$ , and  $(T_{\text{low}}, \log g_{\text{low}})$ , where  $T_{\text{low}} \leq T_{\text{inp}} \leq T_{\text{up}}$  and  $\log g_{\text{low}} \leq \log g_{\text{inp}} \leq \log g_{\text{up}}$ . Next, within each of the 4 nearest models we find the filter-integrated intensities appropriate for  $\mu_{\text{inp}}$ , using linear interpolation. Finally, the desired values of  $I(T_{\text{inp}}, \log g_{\text{inp}}, \mu_{\text{inp}})$  are found by linear interpolation first in the  $\log g$  direction and then the  $T_{\text{eff}}$  direction. Returning the filter-integrated intensities for eight different filters at once is advantageous when modelling observations in several band-passes since one has to search the intensity table only once per surface element per phase.

As we noted above, the technique we just outlined is quite general. We now turn our attention to the recent grid of NEXTGEN models for cool giants computed by PHH using the parallelised version of his general purpose code PHOENIX (Hauschildt et al. 1997). The computational techniques and the input physics used to compute the NEXTGEN models for cool giants have been discussed elsewhere (Hauschildt et al. 1999) and will not be repeated here. These spherical models require an input mass to compute the sphericity factor, and we use  $M = 5 M_\odot$  for all of the models. We did examine a few models

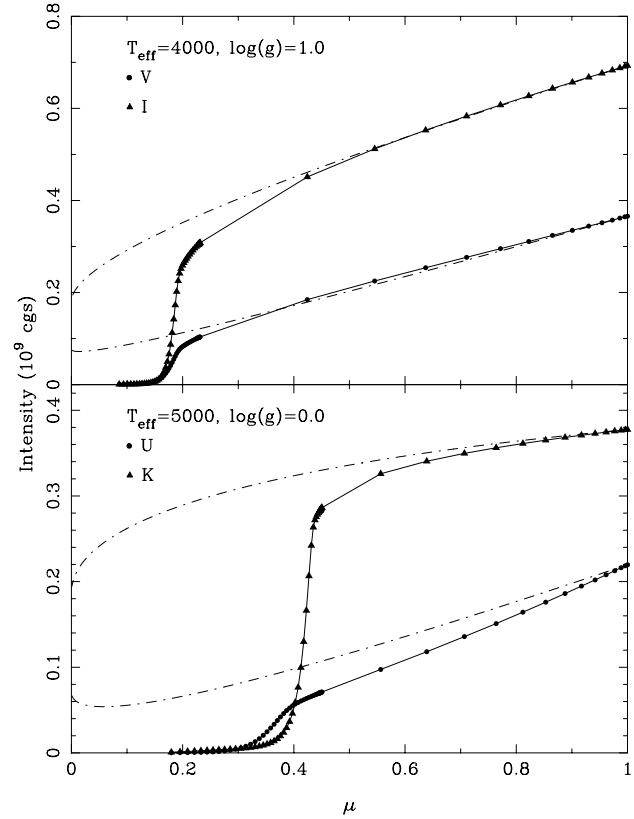


**Fig. 1.** Top: the filter-integrated specific intensities  $I_{\text{FILT}}(\mu)$  for Johnson *V* and *I* for a model with  $T_{\text{eff}} = 4000$  K and  $\log g = 1$ . The dashed-dotted lines show the limb darkening behaviour predicted by the “square root” law (Eq. (4)), where we have used coefficients (computed from Kurucz models) given in Van Hamme (1993). Bottom: the filter-integrated specific intensities  $I_{\text{FILT}}(\mu)$  for Johnson *U* and *K* for a model with  $T_{\text{eff}} = 5000$  K and  $\log g = 0$ , and the corresponding square root limb darkening laws.

with masses of  $2.5 M_\odot$  and  $7.5 M_\odot$  and found no discernible differences compared to the  $M = 5 M_\odot$  models. For the moment we restrict ourselves to the models with solar metallicity. For each model the specific intensities are computed for 64 different angles over a wavelength range of 3000-24,998 Å in 2 Å steps. The distribution of the emergent angles  $\mu$  is chosen by the PHOENIX code based on the structure of the atmosphere under consideration. Hence, in general, the 64 values of  $\mu$  are different from model to model.

Fig. 1 shows the quantity  $I_{\text{FILT}}(\mu)$  for two different NEXTGEN models and filter combinations. The top panel shows the integrated intensities in the Johnson *V* and *I* filters for the model with  $T_{\text{eff}} = 4000$  K and  $\log g = 1.0$  and the bottom panel shows the integrated intensities in the Johnson *U* and *K* filters for the model with  $T_{\text{eff}} = 5000$  K and  $\log g = 0.0$ . For comparison, we also show the square root limb darkening laws (Eq. (4)) computed using coefficients taken from the tabulation of Van Hamme (1993). These four curves essentially show the limb darkening behaviour predicted by the Kurucz models to within a few per cent, although it is important to note that the intensities for  $\mu = 1.0$  are different between the Kurucz

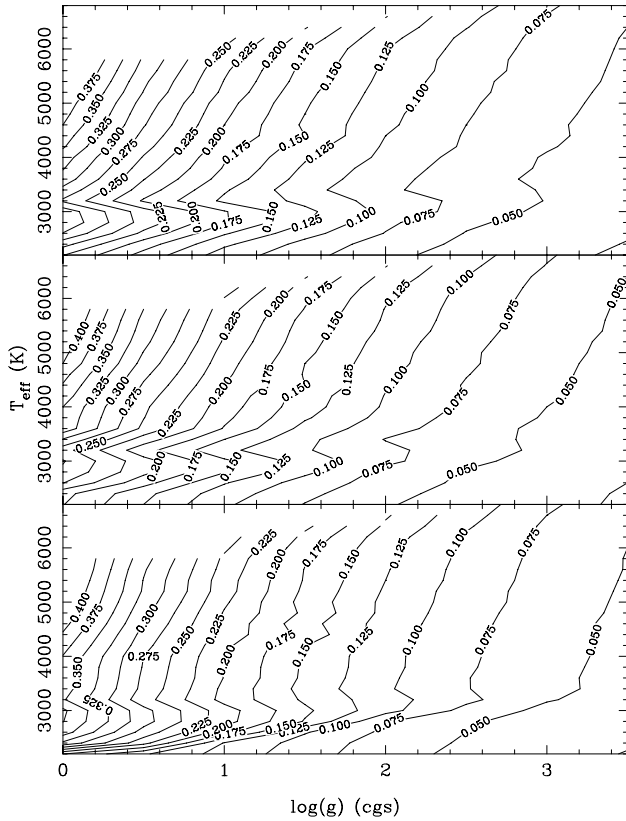


**Fig. 2.** Contour plots of the quantity  $\mu_{\text{cut}}$  for the NEXTGEN models in the *B* (top), *I* (middle), and *K* (bottom) bands. There are no static models for the highest temperatures and lowest gravities, hence there are gaps in the upper left parts of the contour maps.

models and the NEXTGEN models (see Hauschildt et al. (1999) for further discussion of this point). This figure is quite striking. It shows the radically different limb darkening behaviour predicted by the spherical NEXTGEN models and the plane-parallel Kurucz models. The NEXTGEN model predicts a sharp decrease in the intensity at relatively large  $\mu$  values (as large as  $\approx 0.4$ ), whereas the limb darkening parameterisations predict substantial intensity all the way to  $\mu = 0$ . This sudden decrease in the intensity is a consequence of the spherical geometry: for sufficiently low gravities ( $\log g \lesssim 3.5$  for most temperatures) there is much less material near the limbs and hence much less radiation. The radiation that would have come out near the limb in the redder bandpasses comes out at much shorter wavelengths (see Hauschildt et al. 1999).

The value of  $\mu$  where the sudden fall-off in the intensities occurs depends on the effective temperature and gravity of the stellar model, and on the bandpass. We define the slope of the intensities at  $\mu(i)$  to be

$$s(i) = \frac{I(i+1) - I(i-1)}{\mu(i+1) - \mu(i-1)} \quad (11)$$

The location  $\mu_{\text{cut}}$  of the edge is defined to be the point where  $s(i)$  is the largest. Fig. 2 shows contour plots of  $\mu_{\text{cut}}$  for three different bands (Johnson *B*, *I*, and *K*). In general, for a fixed effective temperature,  $\mu_{\text{cut}}$  gets larger as the gravity of the model

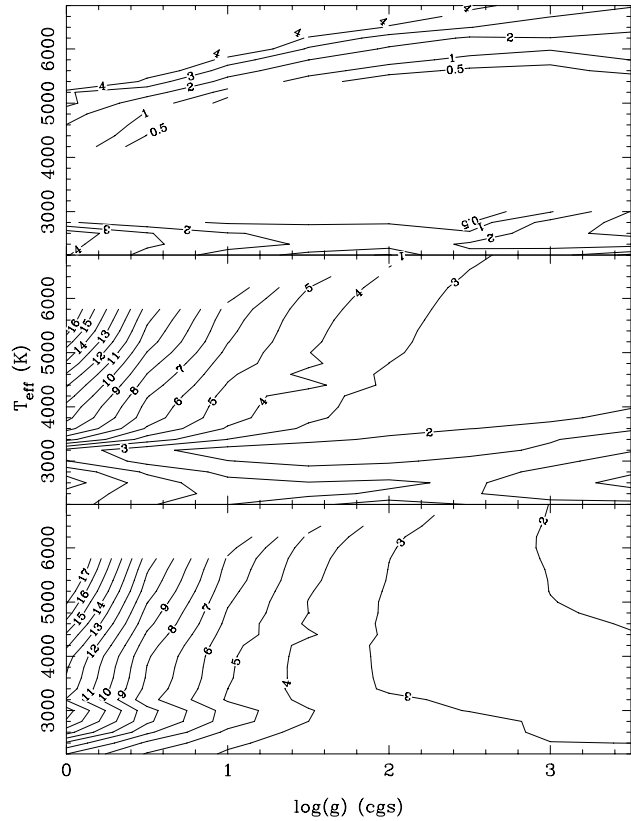


**Fig. 3.** Contour plots of the “lost light,” expressed as a per cent, of the NEXTGEN models in the *B* (top), *I* (middle), and *K* (bottom) bands. There is a large area of the parameter space for the *B* filter (shown as the large gap in the contours) where there is no lost light as defined in the text.

decreases. Also, for a fixed  $\log g$ , the hotter models tend to have a slightly larger values of  $\mu_{\text{cut}}$ . There is some irregular behaviour seen in the contours of  $\mu_{\text{cut}}$  at temperatures between about 3000 K and 4000 K. The reason for this seems to be that for models in this temperature range, the fall-off in the intensity is generally less sudden, especially in the bluer filters. Thus  $\mu_{\text{cut}}$  is less clearly defined in these cases.

It is quite obvious that the quantity  $I_{\text{FILT}}$  (Eq. (9)) evaluated for the NEXTGEN intensities will be less than the corresponding quantity evaluated for a one- or two-parameter limb darkening law. For each model and filter, we computed the “lost light” in the following way. We first “linearised” our table of NEXTGEN intensities: We fitted a line to the intensities for the ten specific angles nearest to  $\mu = 1.0$ . Then the specific intensities for the remaining 54 angles were replaced by the intensities determined from the extrapolation of the fitted line. In most cases, the extrapolated intensities at the limb were above zero. There were a few cases such as the  $T_{\text{eff}} = 5000$ ,  $\log g = 0.0$  *U*-band model shown in Fig. 1 where the extrapolated intensities at the limb would have been negative. In such cases we replaced all negative intensities with zero. Eq. (9) was evaluated for the linearised table and the regular table, and we define the lost light as  $D(T_{\text{eff}}, \log g) = 100 \times (I_{\text{FILT,linear}}(T_{\text{eff}}, \log g) - I_{\text{FILT,regular}}(T_{\text{eff}}, \log g)) / I_{\text{FILT,linear}}(T_{\text{eff}}, \log g)$ . Fig. 3 shows contour plots of

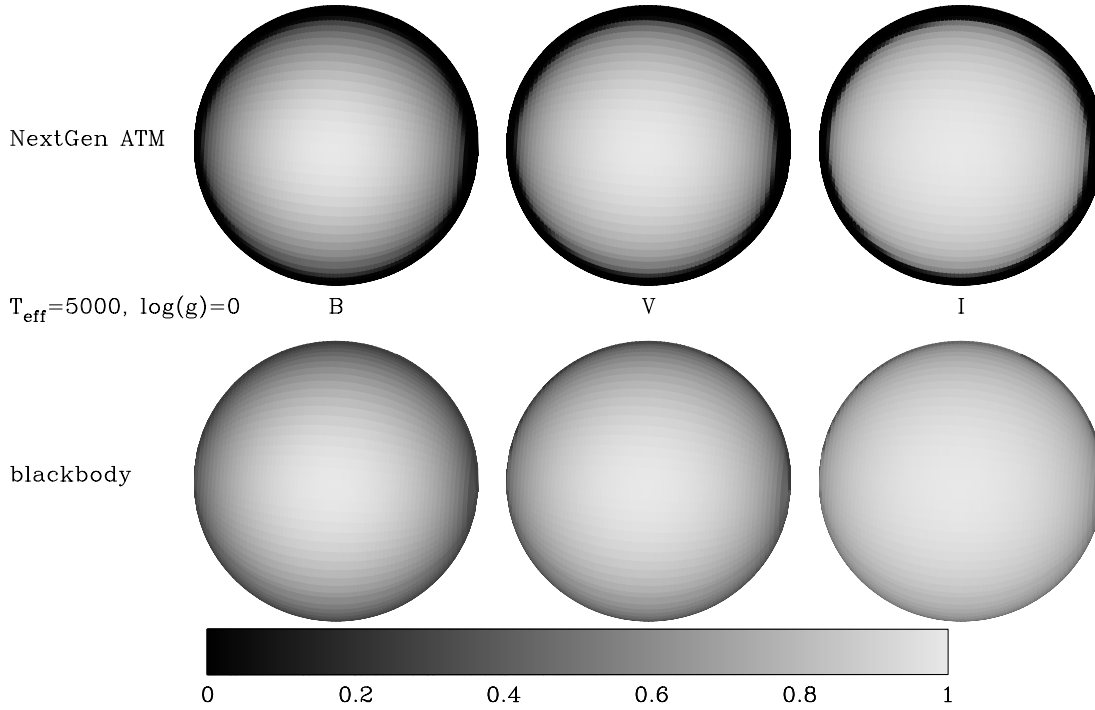


**Fig. 4.** Intensity maps for a spherical star with  $T_{\text{eff}} = 5000$  K and  $\log g = 0.0$ . The top images show intensities computed from the NEXTGEN models in the Johnson  $B$ ,  $V$ , and  $I$  bandpasses, while the bottom images show monochromatic black body intensities with the square root limb darkening law (Eq. (4)) at the effective wavelengths of the same three filters. In each case the intensities have been normalised to 1.0 at the disk centre.

$D(T_{\text{eff}}, \log g)$  for the  $B$  (top),  $I$  (middle), and  $K$  (bottom) filters. By our definition the lost light in many of the  $B$ -band models is zero. Otherwise, for the  $B$  band, the lost light is typically a few per cent and about 3 or 4 per cent for the hottest models. On the other hand, the lost light in the  $I$  and  $K$  bands can be quite substantial, up to 17 per cent for the models with lowest gravities and the hottest temperatures.

We can easily make an image of the disk a model star as it would appear in the sky. The intensity maps displayed in Fig. 4 compare the NEXTGEN intensities for  $T_{\text{eff}} = 5000$  K and  $\log g = 0.0$  to monochromatic black body intensities (limb darkened using the square root law (Eq. (4)) for three different filters (Johnson  $B$ ,  $V$ , and  $I$ ). The star with the NEXTGEN intensities appears smaller on the sky. The difference in the limb darkening closer to the disk centre is also apparent from the figure.

Finally, for comparison purposes, we generated an intensity table from Kurucz models. We retrieved the file “ip00k2.pck19” from Kurucz’s public World Wide Web pages<sup>1</sup>. This file contains the specific intensities for 17 different angles for a grid of solar abundance models. The coolest models have  $T_{\text{eff}} = 3500$  K. All of these models are plane-parallel and LTE.

### 3. General results

We have written a new light curve synthesis code which is based on the work of Avni (Avni & Bahcall 1975; Avni 1978). This

code, named ELC, can model any semi-detached or detached binary with a circular orbit (we will generalise the code to include overcontact binaries and binaries with eccentric orbits within the next year). The second star can be surrounded by an accretion disk. We will defer giving specific details of the code to the Appendix and now turn our attention to the results related to the use of the NEXTGEN intensities.

#### 3.1. Light curve amplitude

For various test cases we computed light curves in four different ways: using our ELC code in the black body mode, using the W-D code in the black body mode (we have added a phase shift of 0.5 to the W-D models, see the Appendix), using our ELC code with the Kurucz intensity table, and using our ELC code with the NEXTGEN intensity table. Fig. 5 shows four different normalised light curves (in  $V$ ,  $I$ , and  $K$ ) for a single Roche lobe filling star in synchronous rotation with  $T_{\text{eff}} = 4000$  K and  $\log g = 1.0$ . The mass ratio is 5, meaning the unseen second star is five times more massive than the cool giant. The inclination is 75 degrees. For the black body models we used the square root limb darkening law with coefficients from Van Hamme (1993). The gravity darkening exponent was  $\beta = 0.08$ , appropriate for a star with a convective envelope. (We note that the black body light curves were computed using a single limb darkening law for the entire star, whereas the light curves computed using model atmosphere intensities (NEXTGEN or Kurucz) will have location-specific limb darkening “built in”.) In all three cases,

<sup>1</sup> <http://cfaku5.harvard.edu/>

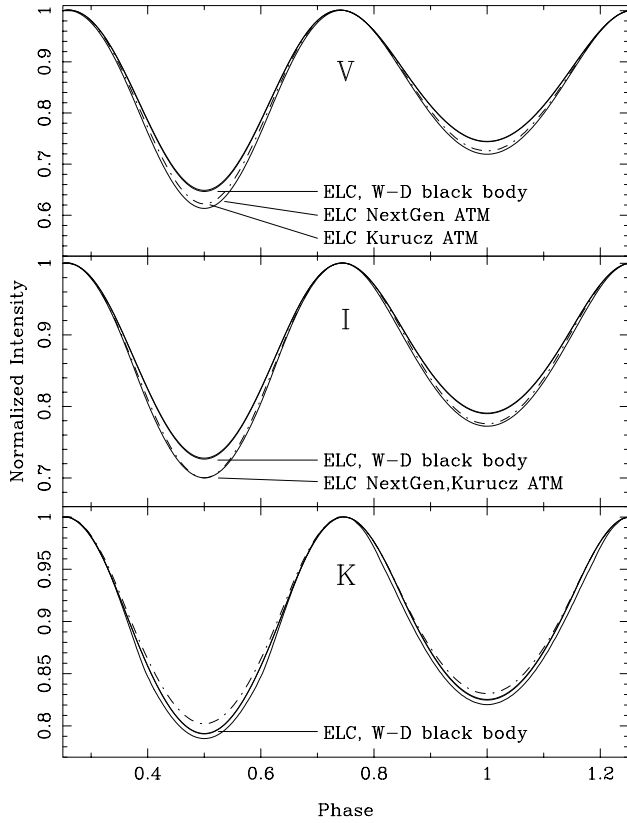


**Fig. 5.** Top:  $V$ -band light curves for a single Roche lobe filling star computed in four ways. The mean temperature of the star is  $T_1 = 4000$  K, its surface gravity is  $\log g = 1.0$ , the binary mass ratio is  $Q = 5$ , and the inclination is  $i = 75$  degrees. The  $y$ -axis is an intensity scale. The two curves with the largest intensities at phase 0.5 are the ELC and W-D monochromatic curves computed using black body intensities (the two curves are nearly identical). The curve in the middle drawn with the dash-dotted line is the light curve generated by ELC using the Kurucz intensity table. The curve with the lowest intensity at phase 0.5 is the ELC curve computed using the NEXTGEN intensities. Middle: Same as the top, but for the  $I$  filter. In this case the curves computed using the Kurucz and NEXTGEN intensities are nearly the same. Bottom: Same as the top, but for the  $K$  filter. The ELC NEXTGEN curve has the deepest minimum at phase 0.5.

the two black body curves are nearly identical (the largest deviations between the two are on the order of 2 millimags). Typically the NEXTGEN curves have deeper minima than the black body curves. Depending on the filter, the NEXTGEN light curves are different from the light curves computed with Kurucz intensities, although for the example shown in Fig. 5 the two  $I$ -band curves have only minor differences.

In general, the light curves computed using the NEXTGEN intensity table are different from light curves computed using the same geometry but with black body intensities. This comes as no surprise, given the potentially large differences in the limb darkening between the NEXTGEN models and the one- or two-parameter limb darkening laws. It is usually the case (especially in the  $I$ ,  $J$ ,  $H$ , and  $K$  filters) that the NEXTGEN light curves have larger amplitudes (in normalised intensity or in magni-

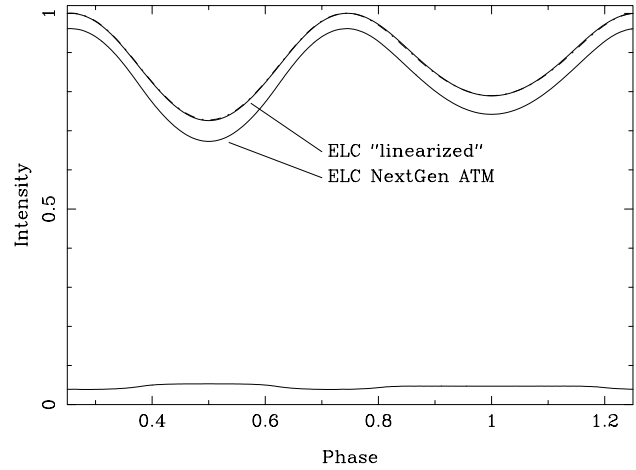


**Fig. 6.** The top curve is the  $I$ -band light curve for a single Roche lobe filling star with  $T_{\text{eff}} = 4000$  K and a mean gravity of  $\log g = 1.0$  constructed using the “linearised” intensity table. As in Fig. 5,  $i = 75^\circ$  and  $Q = 5$ . The  $I$ -band black body light curve shown in Fig. 5 is overplotted with the dash-dotted line (there is essentially no difference between the two curves). The middle curve is the light curve made using the regular NEXTGEN intensity table, plotted on the same intensity scale. The bottom curve is the difference between the linearised curve and the regular curve.

tudes) than the corresponding black body light curves. Fig. 6 shows why this is so. The top curve is the  $I$ -band light curve of the single star described in the Fig. 5 caption made with the linearised intensity table. Since the square root limb darkening law for this model ( $T_{\text{eff}} = 4000$ ,  $\log g = 1.0$ ) and band-pass closely matches the actual NEXTGEN intensities near disk centre (see Fig. 1), the corresponding black body light curve is nearly identical to the “linearised” light curve. The middle curve in Fig. 6 is the light curve for the same star made with the regular NEXTGEN intensity table, plotted on the same intensity scale. The average light level in this light curve is about 5 per cent lower than the linearised one, which is roughly what we would expect from Fig. 3. The bottom curve is the difference between the two top light curves. This lower curve is basically the light lost near the limb, and it is essentially constant with phase. The two top curves have roughly the same amplitude in these intensities units. That is,  $I_{\text{max}} - I_{\text{min}}$  is the same for both curves. However, the *relative* amplitude  $(I_{\text{max}} - I_{\text{min}})/I_{\text{ave}}$  for the regular NEXTGEN light curve will be larger since its mean light level is lower. Hence, the amplitude of this particular NEXTGEN light curve (and most others) in *normalised intensity or in magnitudes* is larger than the amplitude of the corresponding black body curve.

There are some situations such as the  $U$  model shown in the bottom of Fig. 1 where the square root limb darkening law does not match the slope of the NEXTGEN intensities near  $\mu = 1$ . For cases like this, the black body light curve can have a larger amplitude than the NEXTGEN light curve.

Fig. 5 nicely shows the difference in the light curves between black body intensities and model atmosphere intensities (e.g. either NEXTGEN or Kurucz). However, in the example shown,

the NEXTGEN light curves and the Kurucz light curves had only minor differences. To illustrate how large the difference between a NEXTGEN light curve and a Kurucz light curve can be we consider a binary similar to RZ Scuti. This semidetached binary consists of a B3Ib star which rotates near its centrifugal limit and a Roche lobe-filling A2? star (e.g. Olson & Etzel 1994). The mean gravities of the two stars are  $\log g_1 \approx 3.2$  and  $\log g_2 \approx 2.4$ , so sphericity effects should be important here. As a result of its rapid rotation near the critical limit (see Van Hamme & Wilson 1990 for a discussion of “critical rotation”), the B-star is significantly flattened. Furthermore, the surface gravity near its equator is relatively low, giving rise to a relatively large range in temperatures owing to the increased gravity darkening. We currently cannot model the real RZ Scuti binary using the NEXTGEN intensities because the mean temperature of the B-star is well outside our current model grid. Indeed, there are parts on the B-star where the temperature and gravity combination fall outside the Kurucz grid, so we cannot model the real binary with the Kurucz grid either. For this example we therefore modified the temperatures of the two stars and “slowed down” the mass gaining primary slightly so that the temperature and gravity combination of each point on each star is contained in both the NEXTGEN and Kurucz grids. The adopted model parameters are summarised in the caption of Fig. 7. Fig. 7 itself shows the difference between the NEXTGEN light curve and the Kurucz light curve *in magnitudes* for three filters. There are large differences between the two models, and the size of the difference depends on the filter bandpass. The difference between *K*-band light curves is as large as 0.05 mag near phase 0, when the cooler star is eclipsed by the hotter star. One can also note from Fig. 7 that the *U* and *V* difference curves have means which are less than zero. In other words the binary is *bluer* in  $U - K$  and  $V - K$  when NEXTGEN intensities are used compared to when Kurucz intensities are used.

To quantify how much the difference in the light curve amplitudes between the NEXTGEN models and the black body models might matter when fitting the light curves of a real binary star, we consider a model binary similar to T Coronae Borealis. T CrB is an S-type symbiotic binary where an M4 giant orbits an optically faint hot companion with a period of about 227.6 days (Kraft 1958; Kenyon & Garcia 1986; Fekel et al. 2000). There are no eclipses observed in the UV (Selvelli et al. 1992). Nevertheless, the large amplitude of the ellipsoidal light curves suggests the M giant fills its Roche lobe and is viewed at a large inclination (Bailey 1975; Lines et al. 1988; Yudin & Munari 1993). Since the density of a Roche lobe filling star is a function only of the orbital period to a good approximation (Faulkner et al. 1972; Eggleton 1983), the surface gravity of the M giant is only a weak function of its assumed mass. In the case of T CrB,  $\log g \approx 0.7$ , so we expect the sphericity effects to be important here. The mass ratio of the binary is not well known. Kraft (1958) measured hydrogen emission line radial velocities on seven plates and found  $M_{\text{giant}}/M_{\text{comp}} \approx 1.4$ . However, this mass ratio implies a rotational velocity of  $V_{\text{rot}} \sin i \approx 23 \text{ km s}^{-1}$ , which is much larger than the upper limit of  $\approx 10 \text{ km s}^{-1}$  measured by Kenyon & Garcia (1986). We discuss below some

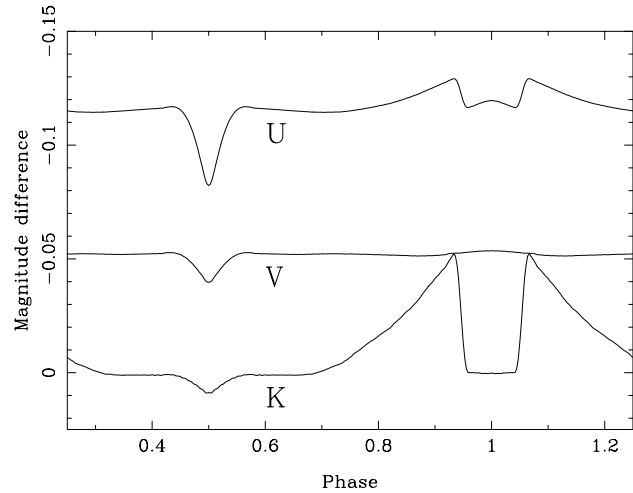


**Fig. 7.** The difference curves *in magnitudes* between the NEXTGEN light curves and the Kurucz light curves for a binary with a geometry similar to RZ Scuti (i.e. a Roche lobe-filling “cool” star and a “hot” mass-gaining star rotating near its critical limit), but with altered temperatures. The adopted parameters are:  $i = 85.65^\circ$ ,  $Q = 0.216$ ,  $P = 15.2$  days,  $a = 61.89 R_\odot$ ,  $T_1 = 6000$  K,  $T_2 = 5000$  K,  $f_1 = 0.66045$ ,  $f_2 = 1.0$ ,  $\Omega_1 = 4$ ,  $\Omega_2 = 1$ ,  $\beta_1 = 0.25$ ,  $\beta_2 = 0.08$ , and detailed reflection with albedos of 1.0 and 0.5 for the hotter and cooler star, respectively (see the Appendix for a detailed discussion of the free parameters of the model). The resulting physical masses, radii, and mean gravities of the two stars are  $M_1 = 11.3 M_\odot$ ,  $R_1 = 14.4 R_\odot$ ,  $\log g_1 = 3.17$  and  $M_2 = 2.45 M_\odot$ ,  $R_2 = 16.2 R_\odot$ ,  $\log g_2 = 2.42$ , respectively.

of the potential problems associated with measuring the rotational velocity of a tidally distorted cool giant, and in view of this discussion the rotational velocity upper limit of Kenyon & Garcia (1986) should be treated with caution.

The *J* and *K* band light curves of T CrB collected between 1987 August and 1995 June are stable and representative of the true ellipsoidal modulation (Yudin & Munari 1993; Shahbaz et al. 1997). The full amplitude of the *J* light curve is about 0.2 magnitudes. On the other hand, the *V* light curve shows additional sources of variability not associated with the underlying ellipsoidal modulation (e.g. Lines et al. 1988). Nevertheless, between about 1989 and the beginning of 1996, the *V* light curve seemed to be reasonably stable. Hric et al. (1998) refer to this period as the “quiet stage”. The full amplitude of the *V* light curve during this quiet stage is about 0.4 magnitudes. For this discussion we will assume this light curve represents the true ellipsoidal light curve. Both Shahbaz et al. (1997) and Belczyński & Mikolajewska (1998) had difficulty fitting the optical (*V* or *I*) light curves simultaneously with the infrared (*J* or *K*) light curves. If the amplitude of the *J* band light curve was matched, then the model *V* and *I* light curves (computed using black body intensities) had amplitudes that were about a factor of two too small.

A thorough analysis of existing T CrB data is beyond the scope of the present paper and will be deferred to a future paper. For now it will suffice to discuss simulated T CrB-like light curves. For these light curves we will use the T CrB

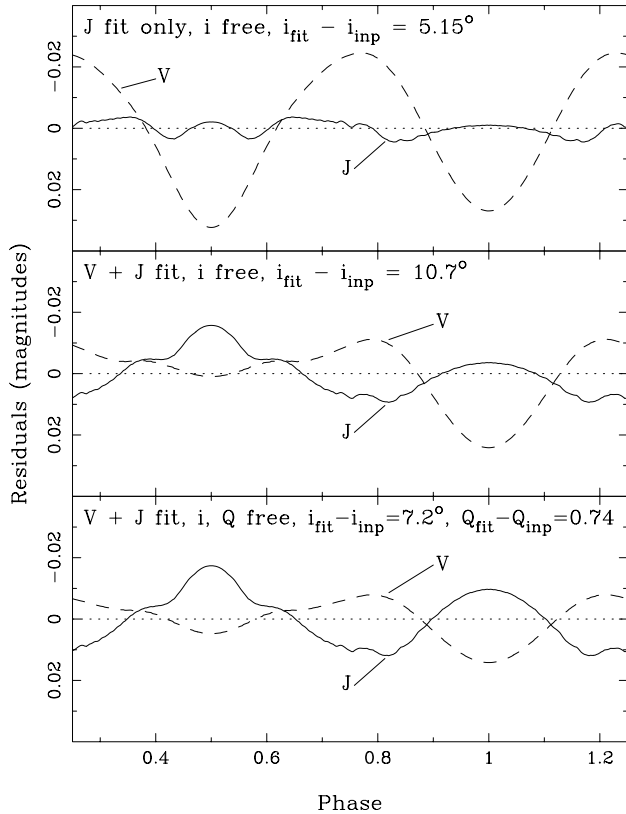


**Fig. 8.** The results of fitting a NEXTGEN light curve using black body intensities. The input model parameters are single Roche lobe-filling star,  $T_{\text{eff}} = 3560$  K,  $Q = 1.6666$ , and  $i = 60^\circ$ . Top panel: the  $O - C$  residuals (in magnitudes) of a fit to the  $J$ -band light curve only ( $Q$  fixed,  $i$  free). The fitted inclination is  $i = 65.15^\circ$ , and the amplitude of the  $V$ -band light curve is nearly 0.03 magnitudes too small. Middle panel: similar to top, but a fit to both  $V$  and  $J$ . The fitted inclination is nearly  $11^\circ$  too large, and the  $V$  residuals still have relatively large systematic deviations. Bottom panel: similar to the middle, but both the inclination and mass ratio were free parameters. The residuals are reasonably small, but the fitted parameters are quite different from the input parameters.

system parameters adopted by Belczyński & Mikolajewska (1998), namely  $M_{\text{giant}}/M_{\text{comp}} = 0.6$ , which in our notation is  $Q = 1/0.6 = 1.6666$ ,  $i = 60^\circ$ ,  $T_{\text{eff}} = 3560$  K, and a gravity darkening exponent of  $\beta = 0.08$ , appropriate for a star with a convective outer envelope. We also used the orbital period and  $K$ -velocity of the M giant given in Kenyon & Garcia (1986). Using the NEXTGEN intensity table we computed light curves for the Johnson  $V$  and  $J$  filters. The model light curves were converted to magnitudes for compatibility with our optimising routines. We used ELC in its black body mode to fit various combinations of the simulated light curves, and the results are shown in Fig. 8. The top panel shows the results of fitting the  $J$  light curve only, using the inclination as the sole free parameter. The fitted inclination is  $65.15^\circ$ , and the  $O - C$  residuals for the  $J$  band are reasonably small ( $\lesssim 0.01$  mag). However, if we take the predicted  $V$  light curve for this geometry and compare it to the simulated  $V$  light curve, we find that

the amplitude of the black body  $V$  light curve is much *smaller* than the amplitude of the simulated  $V$  (NEXTGEN) light curve. Thus we have reproduced the same problem that Shahbaz et al. (1997) and Belczyński & Mikolajewska (1998) had when they attempted simultaneous optical and infrared fits. Not surprisingly, if we attempt to fit both our simulated  $V$  and  $J$  light curves simultaneously using the inclination as the only free parameter, the fits to the  $J$  light curve get worse (middle panel). Finally, we fit both light curves simultaneously using both the inclination and mass ratio as free parameters. The  $O - C$  residuals for both filters are not excessively large and might be comparable to the observational errors in the real binary. However, the fitted parameters are quite different from the input ones:  $Q_{\text{fit}} = 2.41$  and  $i_{\text{fit}} = 67.2^\circ$ , compared to input values of  $Q_{\text{inp}} = 1.67$  and  $i_{\text{inp}} = 60.0^\circ$ . Naturally, the derived component masses from the fit are significantly different from the input masses:  $M_{\text{giant}}(\text{fit}) = 0.32 M_\odot$  and  $M_{\text{comp}}(\text{fit}) = 0.78 M_\odot$ , compared to input values of  $M_{\text{giant}}(\text{inp}) = 0.71 M_\odot$  and  $M_{\text{comp}}(\text{inp}) = 1.18 M_\odot$ .

### 3.2. Rotational broadening kernels

Measurements of the rotational velocities of the stars in close binaries provide powerful constraints on the light curve solution. Indeed, any light curve solution that specifies the mass ratio, inclination, and the angular velocity ratios predicts specific values for the observed values of  $V_{\text{rot}} \sin i$ , provided of course that at least one radial velocity curve is available. In cases where a star fills its critical lobe exactly and is in synchronous rotation (generally safe assumptions in cataclysmic variables and low mass X-ray binaries), a measurement of its rotational velocity constrains the mass ratio of the binary (e.g. Wade & Horne 1988).

If spectra with high resolution and high signal-to-noise are available, then one can use Fourier techniques to measure the rotational velocity (e.g. Gray 1992 and cited references). When only spectra of lower quality are available, then often one measures  $V_{\text{rot}} \sin i$  by comparing the spectrum of interest with a spectrum of a slowly rotating template star (observed with similar instrumentation) that has been convolved with a broadening kernel  $G(\lambda)$ . Various trial values of the width of the broadening kernel are tried until the optimal match is found. Gray (1992, pp. 370-374) gives a clear description of how to compute the broadening kernel  $G(\lambda)$  analytically for the case where the intrinsic line profile  $H(\lambda)$  has the same shape over the entire disk. Essentially, one can place an  $x, y$  coordinate system on the apparent disk of the star on the sky where the  $y$ -axis is parallel to the axis of rotation. The disk of the star can then be divided up into a number of strips parallel to the  $y$ -axis, each having its own Doppler shift according to its  $x$ -coordinate. The broadening kernel is evaluated at a particular Doppler shift by integrating the intensity over the appropriate strip. Normally one assumes a linear limb darkening law with a coefficient of  $x = 0.6$  when computing  $G(\lambda)$ . Finally, the broadened line profile is the convolution of the intrinsic line profile with the kernel:  $H_{\text{rot}}(\lambda) = G(\lambda) * H(\lambda)$ .

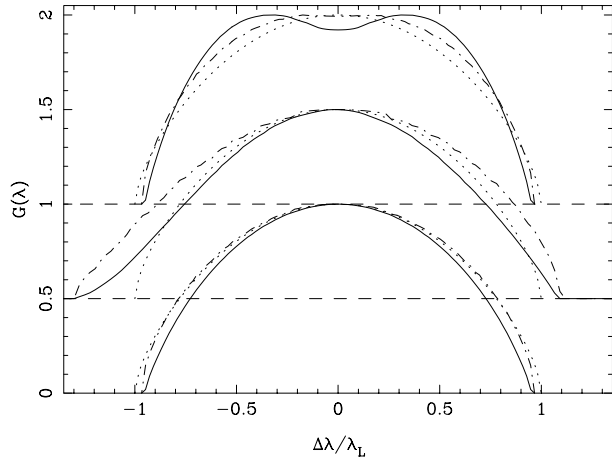


**Fig. 9.** Rotational broadening kernels  $G(\lambda)$  for the star described in the caption to Fig. 5 for three different phases:  $0.0$  (lower curves),  $90^\circ$  (middle curves, offset by  $0.5$ ), and  $180^\circ$  (upper curves, offset by  $1.0$ ) (the giant is behind its invisible companion at phase  $180^\circ$ ). The solid lines are the kernels for Roche geometry and NEXTGEN intensities. The dash-dotted curves are for Roche geometry and black body intensities plus a linear limb darkening law with a coefficient of  $x = 0.6$ . The dotted curves are analytic kernels with a limb darkening coefficient of  $0.6$ .

The above discussion applies to spherical stars. A star that fills a substantial fraction of its Roche lobe departs markedly from spherical symmetry, and as such will have distorted line profiles (e.g. Kopal 1959; Marsh et al. 1994; Shahbaz 1998). Furthermore, the degree of the line profile distortion depends on the Roche geometry (i.e. mass ratio and inclination) and the orbital phase (Shahbaz 1998). The intensity maps that the ELC program can write (e.g. Fig. 4) can be used to numerically evaluate  $G(\lambda)$ , thereby accounting for both the nonspherical shape of the star and the nonlinear limb darkening. Fig. 9 shows rotational broadening kernels  $G(\lambda)$  for the star described in the caption to Fig. 5 for phases  $0.0$ ,  $90^\circ$ , and  $180^\circ$ , when the giant is behind its invisible companion. The situation is complicated. Near phase  $0.0$ , the projected surface of the giant in the plane of the sky is not too different from a circle (it is flattened slightly in the  $y$ -direction). Thus the observed profile will be nearly symmetric. However, the kernel, computed using the NEXTGEN intensities, is *narrower* than the analytic kernel and the kernel computed using black body intensities and linear limb darkening since the star with the NEXTGEN intensities appears smaller on the sky (Fig. 4). At phase  $90^\circ$  (quadrature), the star is elongated in the  $x$ -direction. As a result, the broadening kernel computed from the black body intensities is *wider* than the analytic kernel, and it is asymmetric. As a result of the sharp cut-off in the limb darkening, the kernel computed using the NEXTGEN intensities is narrower than the black body kernel. However, for this particular situation, the NEXTGEN kernel has roughly the same width as the analytic kernel. Finally, at phase  $180^\circ$ , when the giant is behind its unseen companion, all three kernels have more or less the same full width at half maximum. However, the kernel computed using the black body intensities is flat-topped (Shahbaz (1998) also noted absorption line profiles with flat

bottoms near this phase (his Fig. 1)), and the kernel computed with the NEXTGEN intensities has a local minimum at zero velocity. The reason the kernels have flat tops or even central depressions near phase  $180^\circ$  is quite straightforward. The  $L_1$  point is in full view near this phase, and for high inclinations there are no points on the apparent stellar disk with  $\mu = 1$ . For the example shown in Fig. 9,  $\mu < 0.924$  everywhere on the star at phase  $180^\circ$ . Hence the central parts of the apparent stellar disk are fainter (owing to limb darkening) than they would have been in the spherical case and there is less contribution to the kernel near zero velocity. If the intensities are computed using the NEXTGEN table and the gravity is sufficiently low, then the central part of the star can be even darker. In some cases such as the one shown in Fig. 9, the  $L_1$  point will be so dark that the broadening kernel will actually have a central depression near zero velocity.

Given the variety of distortions in the broadening kernel as shown in Fig. 9, it would be prudent to compute phase-specific broadening kernels when extracting  $V_{\text{rot}} \sin i$  measurements from spectra (see also Shahbaz 1998). As a specific example, we consider the eclipsing binary UU Cancri, which consists of a K giant in a 96.7 day orbit about an essentially invisible (in the optical) companion (e.g. Eaton et al. 1991). There is good evidence for an accretion disk around the unseen companion (Zola et al. 1994), so we will assume that the K giant fills its Roche lobe exactly and that it is in synchronous rotation. Eaton et al. (1991) obtained a series of high resolution spectra and noted a change in the Doppler broadening of certain metallic absorption lines as a function of phase. This behaviour is consistent with expectations (Shahbaz 1998). Using a linear limb darkening law with  $x = 0.85$ , Eaton et al. (1991) determined a rotational velocity of  $V_{\text{rot}} \sin i = 25 \pm 1$  km s $^{-1}$  for a spectrum near a quadrature phase and derived a mass ratio of  $Q = M_{\text{comp}}/M_{\text{giant}} \approx 1.2$  (using ELC, we derive a mass ratio  $Q = 1.235$  from  $V_{\text{rot}} \sin i = 25 \pm 1$ , where we have adopted a mass function for the unseen companion of  $f(M) = 0.56 M_\odot$  (Popper 1977)). We plot in Fig. 10 the analytic broadening kernel for  $x = 0.85$  and a mean rotational velocity of  $2\pi R_{\text{eff}}/P = 25$  km s $^{-1}$ , where  $R_{\text{eff}}$  is the sphere-equivalent Roche lobe radius. We also show a broadening kernel computed using NEXTGEN intensities, assuming  $Q = 1.65$  and  $2\pi R_{\text{eff}}/P = 20.7$  km s $^{-1}$ . We have adopted an inclination of  $i = 89.6^\circ$  and an effective temperature of 3900 K for the K giant (Zola et al. 1994). The two broadening kernels have nearly the same full width at half maximum. However, the implied component masses for the two cases are quite different. Assuming  $i \approx 90^\circ$ ,  $Q = 1.235$  (the value from Eaton et al. 1991) implies  $M_{\text{giant}} = 1.49 M_\odot$ ,  $M_{\text{comp}} = 1.83 M_\odot$ , and  $\log g_{\text{giant}} = 1.25$ , whereas our value of  $Q = 1.65$  gives  $M_{\text{giant}} = 0.88 M_\odot$ ,  $M_{\text{comp}} = 1.44 M_\odot$ , and  $\log g_{\text{giant}} = 1.19$ . Zola et al. (1994) find a photometric mass ratio from their light curve solutions of  $q = M_{\text{giant}}/M_{\text{comp}} = 0.564 \pm 0.006$ , which in our notation is  $Q = 1.77 \pm 0.01$ . The case of UU Cnc is perhaps an extreme example, but it serves to illustrate the importance of using broadening kernels which account for deviations from linear limb darkening and spherical geometry.

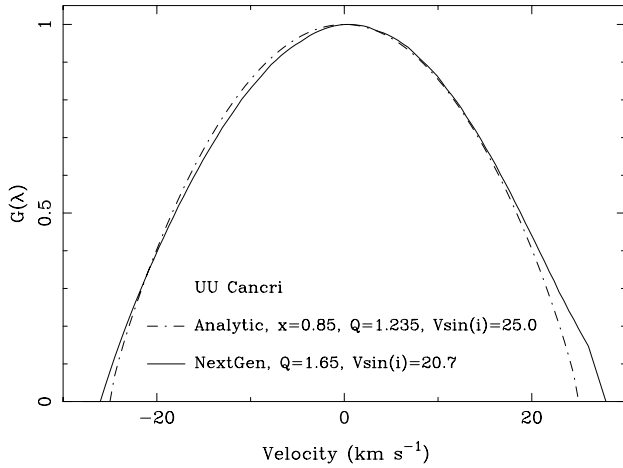


**Fig. 10.** Rotational broadening kernels  $G(\lambda)$  for UU Cancri. The solid line is the kernel computed for a mass ratio of  $Q = 1.65$ , which corresponds to a “mean” rotational velocity of  $2\pi R_{\text{eff}}/P = 20.7 \text{ km s}^{-1}$ . The dash-dotted line is the analytic kernel computed by Eaton et al. (1991), corresponding to  $Q = 1.235$  and  $2\pi R_{\text{eff}}/P = 25.0 \text{ km s}^{-1}$ .

### 3.3. Accuracy of the integration and interpolation

Given the relatively large differences in the predicted light curves and broadening kernels that we predict, it is worthwhile to discuss the numerical accuracy of the output light curves. Since the computation of the NEXTGEN models is somewhat time consuming, we cannot tabulate models for all effective temperatures and gravities. We have done extensive testing on the integration and interpolation procedures, and we believe the present table (steps of 0.5 dex in  $\log g$  and 200 K in  $T_{\text{eff}}$ ) is a reasonable compromise between CPU time and sampling accuracy. There are various ways to see how “smooth” the filter-integrated intensities are as a function of the effective temperature and gravity. Figs. 11 and 12 show two such representations. In Fig. 11 we show as a function of the gravity the integrated  $I$ -band intensity for four effective temperatures (4000, 4400, 5000, and 5600 K) at six different emergent angles ( $\mu = 0.05, 0.10, 0.15, 0.20, 0.25,$  and  $0.30$ ). In general, these curves are smooth, and a linear interpolation of the intensity in the  $\log g$  direction gives reasonable accuracy. Fig. 12 shows a similar plot, but with the intensities as a function of the effective temperature. As before, the curves are quite smooth and a linear interpolation in  $T_{\text{eff}}$  gives reasonable results. There is some irregular behaviour in the curves for  $\mu = 0.05$  and  $\mu = 0.10$ . In practice, however, the contribution to the overall integrated light curve from angles less than 0.1 is small since the intensities are weighted by the value of  $\mu$ .

Another way to test the accuracy of the interpolation is to leave specific models out of the table, compute a light curve, and compare it to the light curve computed using the full intensity table. Fig. 13 shows results of this exercise for the star described in the caption of Fig. 5. We computed “regular” light curves where we used all models in the intensity table and “cut” light curves where the  $T_{\text{eff}} = 4000, \log g = 1.0$  model was excluded from the table. Thus, at  $T_{\text{eff}} = 4000$ , the local step size in

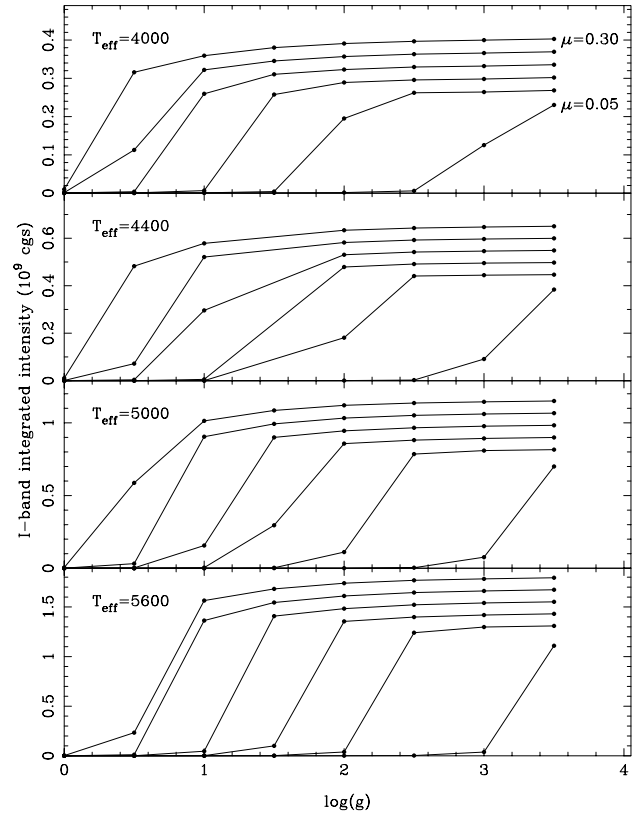


**Fig. 11.** The curves show the integrated  $I$ -band specific intensity for various specific angles and effective temperatures as a function of the effective gravity. The intensity is generally a smooth function for a fixed temperature and emergent angle. Thus a linear interpolation in  $\log g$  is reasonably accurate.

$\log g$  was 1 dex, rather than 0.5 dex. To compare the light curves, we define the “difference curve” as  $D = 100(I_{\text{reg}} - I_{\text{cut}})/I_{\text{reg}}$ , where  $I_{\text{reg}}$  is the integrated light computed using the full intensity table and  $I_{\text{cut}}$  is the integrated light computed using the intensity table with the  $T_{\text{eff}} = 4000, \log g = 1.0$  model removed. We see that the systematic difference between the two curves is usually about 0.3 per cent and is at most 0.75 per cent in  $V$ . The corresponding values for  $I$  and  $K$  are even smaller. We also computed light curves using two different grids of surface elements: the “standard” grid with  $N_{\alpha} = 40$  and  $N_{\beta} = 14$  and the “fine” grid with  $N_{\alpha} = 120$  and  $N_{\beta} = 40$ . Using the fine grid has little effect on the difference curves: the curves are smoother but the overall shapes are the same. The lowermost curve in Fig. 13 compares the regular  $V$  light curve computed using the standard and fine grids. The two curves are the same to within 0.05 per cent (i.e. less than about 0.5 millimag). We conclude that for most situations our regular intensity table and the standard grid are adequate.

There is nothing in our integration and interpolation techniques that limits us to  $\approx 1$  per cent accuracy. Since our interpolation scheme does not have a fixed step size in the temperature or gravity we can easily add a few models with the appropriate temperatures and gravities for special cases where the data demand the highest accuracy. Other light curve codes also suffer

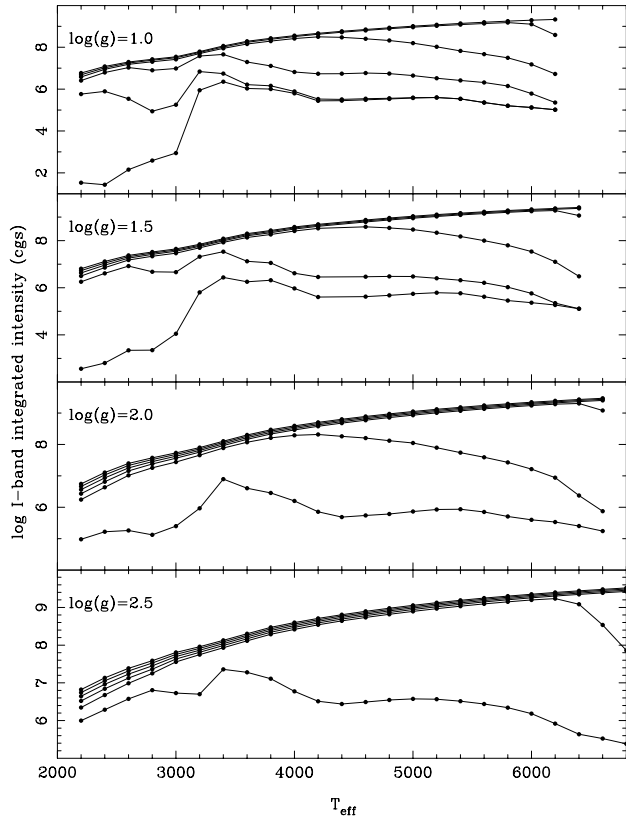


**Fig. 12.** Similar to Fig. 11, except the intensity is now displayed as a function of the effective temperature. Note the  $y$ -axis scale here is logarithmic. Within each panel, the specific angles are from bottom to top  $\mu = 0.05, 0.10, 0.15, 0.20, 0.25,$  and  $0.30$ . In most cases the  $\mu = 0.25$  and the  $\mu = 0.30$  curves are nearly the same. As in Fig. 11, the curves are quite smooth, and a linear interpolation of the intensity in  $T_{\text{eff}}$  is reasonably accurate.

systematic errors on the few per cent level. For example, most versions of the W-D code use a single limb darkening law for the entire star. Since the temperature and gravity are not constant over the surface of a tidally distorted star, small systematic errors can be present when a limb darkening law for a single temperature and gravity are used. Van Hamme & Wilson (1994) have discussed this point in more detail.

#### 4. Discussion and summary

In this paper we have presented a way to include specific intensities from detailed model atmosphere computations into a light curve synthesis code. We have shown that using the model atmosphere intensities directly is almost required for cool giants since the limb darkening behaviour for a cool low-gravity atmosphere is radically different than simple one- or two-parameter limb darkening laws (Fig. 1). This departure from the near-linear limb darkening law is a consequence of the spherical geometry used in the computation of the NEXTGEN models. Other workers have computed spherical model atmospheres for cool giants before (e.g. Scholz & Tsuji 1984; Scholz & Takeda 1987; Plez et al. 1992; Jørgensen et al. 1992), and the strongly non-

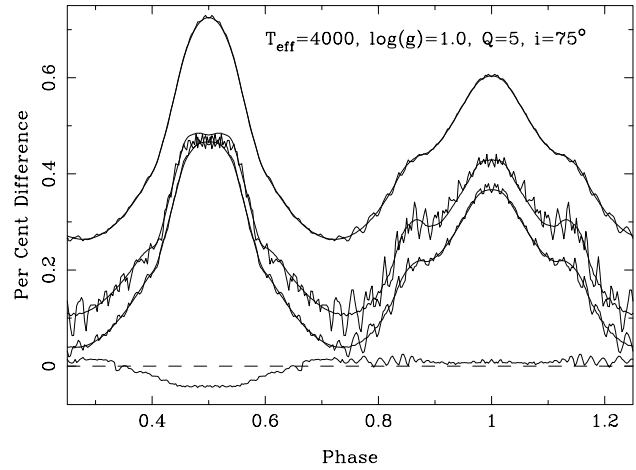


**Fig. 13.** “Difference” plots in the light curves for the star described in the caption to Fig. 5. The top three sets of curves are difference curves for  $V$ ,  $K$ , and  $I$ . For each filter, there are two curves corresponding to a “standard” grid of surface elements ( $N_\alpha = 40$ ,  $N_\beta = 14$ ) and a “fine” grid ( $N_\alpha = 120$ ,  $N_\beta = 40$ ). The curves for the fine grids are smoother. The curve at the bottom compares the regular  $V$  models computed using the two different grids.

linear limb darkening behaviour has previously been noted by Scholz & Takeda (1987), and more recently by Hofmann & Scholz (1998). We have shown that this strongly nonlinear limb darkening has a large effect on the light curve amplitude. In general, the light curves computed using the NEXTGEN intensities have larger amplitudes than the light curves computed using the same geometry but with black body intensities and a one- or two-parameter limb darkening law. Also, the strongly nonlinear limb darkening has an effect on rotational broadening kernels in that for spherical stars the kernel computed using the NEXTGEN intensities will be narrower than a numerical or an analytic kernel that has a linear limb darkening law. If the star fills a substantial fraction of its Roche lobe, then the broadening kernel will also be different than the analytic one owing to the nonspherical shape of the star.

Thus we basically have two different types of models with which to fit close binary light curves: our ELC code with the NEXTGEN intensities, and codes that use either black body intensities or plane-parallel model atmosphere intensities and near-linear limb darkening (e.g. W-D, ELC in black body mode, ELC with the Kurucz table, etc.). It should be possible to test which class of models provides the better description of the observational data available for binaries with cool giants. In this regard, we have shown that observations in several bandpasses are useful in discriminating between the models. For example, Figs. 5 and 7 show how the difference in the depths of the minima between the NEXTGEN and Kurucz light curves depends on the bandpass, while Fig. 8 shows that black body light curves provide a poor simultaneous fit to NEXTGEN  $V$  and  $J$  light curves of a binary like T CrB. There is no shortage of potentially good binary stars to study. For example, T CrB, as we have already noted, has  $V$ ,  $I$ ,  $J$ , and  $K$  light curves available (although the light curves are perhaps somewhat noisy). RZ Ophiuchi is an

eclipsing binary consisting of a hot  $\approx$ B star and a K supergiant. The orbital period is 262 days. Reasonably good light curves in the bluer filters exist (e.g. Knee et al. 1986; Olson 1993), and additional observations in  $J$ ,  $H$ , and  $K$  would be extremely valuable. Kruszewski & Semeniuk (1999) present a catalog of poorly studied eclipsing binaries with good parallaxes measured by the *Hipparcos* mission. Many of these binaries have long periods (more than 10 days) and contain evolved cool components. Needless to say, we encourage observers to systematically study these binaries in multiple colours. With a binary of known distance, one has the added challenge of obtaining the correct integrated flux.

Our interest should not be confined to binaries with a supergiant component. For example, there appears to be a small class of “long period” Algol type binaries (periods between about 10 and 20 days) where the mass losing cool star appears to be slightly underfilling its Roche lobe. Some examples are WW Andromedae (Olson & Etzel 1993a), S Cancri (Olson & Etzel 1993b), and DN Orionis (Etzel & Olson 1995). The cool stars in these three systems have surface gravities near  $\log g \approx 2.5$ , so the sphericity effects are not as pronounced as they are in systems like T CrB. On the other hand, all three of these binaries have excellent five-colour ( $I(Kron)ybvuv$ ) photometry, and S Cnc and DN Ori are totally eclipsing and are double-lined. Olson and Etzel report that in each case, the cool star seems to underfill its Roche lobe by about 10 per cent. It would be worthwhile to re-evaluate the light curve solutions for these three stars using ELC and the NEXTGEN intensities to see if the sphericity effects can account for the apparent slight underfilling of the Roche lobes by the cool stars.

*Acknowledgements.* We thank Marten van Kerkwijk, Frank Verbunt, and Robert E. Wilson for helpful discussions. JAO gratefully acknowledges the hospitality of the Institute of Astronomy in Cambridge. PHH’s work was supported in part by the CNRS, INSU and by NSF grant AST-9720704, NASA ATP grant NAG 5-8425 and LTSA grant NAG 5-3619, as well as NASA/JPL grant 961582 to the University of Georgia. This work was supported in part by the Pôle Scientifique de Modélisation Numérique at ENS-Lyon. Some of the calculations presented in this paper were performed on the IBM SP and SGI Origin 2000 of the UGA UCNS, on the IBM “Blue Horizon” of the San Diego Supercomputer Center (SDSC), with support from the National Science Foundation, and on the Cray T3E and IBM SP of the NERSC with support from the DoE. We thank all these institutions for a generous allocation of computer time.

## Appendix: brief outline of the ELC code

### A.1. Introduction and history

Yorham Avni was interested in, among other things, mass determinations of the compact objects in high mass X-ray binaries (e.g. Cyg X-1, Cen X-3, etc.). During the course of his research he wrote a FORTRAN code to compute the ellipsoidal light curve of a single (usually) Roche-lobe filling star (Avni & Bahcall 1975; Avni 1978). Avni passed on this code to Jeff McClintock and Ron Remillard shortly before his death in March of 1988 (see McClintock & Remillard 1990). The code was

passed on to JAO from Ron Remillard sometime in 1994 when JAO was a graduate student at Yale. During the spring of 1995 it became clear that the black hole binary GRO J1655-40 was an eclipsing system and that the Avni code in its original form was not adequate. The code was substantially modified by JAO in the summer of 1995 to include light from an accretion disk and to account for eclipses (Orosz & Bailyn 1997).

The code described in Orosz & Bailyn (1997) is somewhat unwieldy and it was becoming more and more difficult to read and modify. Therefore a more general and more modular code was developed by JAO. Although we have used much of Avni’s notation, and we have followed his basic method of setting up the Roche geometry and integrating the observable flux, most of the code is new. Owing to space limitations, we cannot give below each equation used. Rather, we give below some details of the parts of the code which have been substantially revised with respect to the earlier versions (there are numerous other papers and texts which go into varying amounts of detail, Wilson & Devinney 1971; Wilson 1979; Avni & Bahcall 1975; Avni 1978; Linnell 1984; Wilson 1990; Orosz & Bailyn 1997).

### A.2. The potential

We assume surface of the star is an equipotential surface of the following potential, which includes the gravitational, centrifugal, and Coriolis forces (Avni & Bahcall 1975):

$$\Psi = \frac{GM_1}{D} \left[ \frac{1}{r_1} + \frac{Q}{r_2} - Qx + \frac{1+Q}{2} \left( \frac{\omega_1}{\omega_{\text{orb}}} \right)^2 (x^2 + y^2) \right] \quad (\text{A.1})$$

where  $M_1$  is the mass of the star under consideration,  $D$  is separation between two stars,  $Q = M_2/M_1$  is the mass ratio,  $\omega_1$  is the star’s rotational angular velocity,  $\omega_{\text{orb}}$  is the orbital angular velocity,  $r_1$  and  $r_2$  are the distances to the stellar centres in units of  $D$ , and  $x$  and  $y$  are normalised coordinates centred at star 1. For a binary with a given mass ratio  $Q$ , rotational angular velocity  $\omega_1$  and orbital angular velocity  $\omega_{\text{orb}}$ , there is a critical value of the potential  $\Psi_{\text{crit}}$  where the star exactly fills its limiting lobe. Stars that are smaller than their limiting lobes will have  $\Psi > \Psi_{\text{crit}}$ .

To fully define the surface of the star, the user specifies  $Q$ ,  $\Omega = \omega_1/\omega_{\text{orb}}$ , and the “filling factor”  $f \equiv x_{\text{point}}/x_{L1}$ , where  $x_{\text{point}}$  is the  $x$ -coordinate of the “nose” of the star and  $x_{L1}$  is the  $x$ -coordinate of the  $L_1$  point. In our case, the filling factor  $f$  is exactly 1 for Roche lobe-filling stars and less than 1 for detached stars. Situations with  $f > 1$  (the contact binaries) are currently not allowed. When  $f < 1$ , the program computes  $x_{\text{point}}$  from  $x_{\text{point}} = fx_{L1}$  and then computes  $\Psi(x_{\text{point}}, 0, 0)$ , which is the adopted potential for the star. Once the surface of the star is defined, a grid of surface elements is made using a polar coordinate system with  $N_\alpha$  latitude rows equally spaced in the angle  $\theta$  and  $4 * N_\beta$  longitude points per latitude row equally spaced in the angle  $\phi$ . (Earlier versions of the code used a cylindrical coordinate system with  $N_\alpha$  rings equally spaced along the line of centres, running from the  $L_1$  point to the back

of the star and  $4 * N_\beta$  surface points per ring equally spaced in angle.) It is convenient to use an internal rectangular coordinate system centred on star 1 where the  $x$  axis points to the centre of the other object and the  $z$  axis is parallel to the direction of  $\omega_1$ . The value of  $\Psi$  and its derivatives are computed for each element, and from these quantities the local gravities  $g(x, y, z)$  and the surface normal vectors follow.

### A.3. Mean temperature vs. polar temperature

The temperature of the secondary star was defined in the Avni code by its polar temperature  $T_{\text{pole}}$ . Given  $T_{\text{pole}}$ , the temperatures of the other surface elements followed from the well-known von Zeipel relation:

$$\frac{T(x, y, z)}{T_{\text{pole}}} = \left[ \frac{g(x, y, z)}{g_{\text{pole}}} \right]^\beta. \quad (\text{A.2})$$

The exponent  $\beta$  is 0.25 for stars with a radiative atmosphere (von Zeipel 1924) and 0.08 for stars with convective envelopes (Lucy 1967). Wilson (1979) has pointed out that the polar temperature and the mean temperature of a distorted star will be different. In most cases, of course, one measures the mean temperature via the spectral type or colour index. Therefore, following Wilson (1979), we now have as input the mean (or equivalently effective) temperature of the star, denoted by  $T_{\text{eff}}$ . The effective temperature is computed from the bolometric luminosity

$$L = \sigma S T_{\text{eff}}^4 \quad (\text{A.3})$$

where  $S$  is the surface area.  $T_{\text{pole}}$  is then given by (Wilson 1979)

$$T_{\text{pole}} = T_{\text{eff}} \left[ \frac{S}{\int_{\text{surface}} g_{\text{norm}}(x, y, z)^{4\beta} dS(x, y, z)} \right]^{1/4} \quad (\text{A.4})$$

where  $g_{\text{norm}}(x, y, z) = g(x, y, z)/g_{\text{pole}}$  and  $dS(x, y, z)$  is an element of surface area (Eqs. (A8), (A9), and (A10) of Orosz & Bailyn 1997).

### A.4. Addition of a second star

Adding a second star to the code is relatively simple. We “flip” the mass ratio (define  $Q' = 1/Q$ ), and solve for the potential and its gradients using the same subroutines as for the first star. When integrating the observed flux, we add  $180^\circ$  to the phase and use the same subroutines as for the first star. One complication occurs when the second star is not in synchronous rotation (Wilson 1979). In this case, the  $x$  derivative of the potential that is used in the detailed reflection routine (see below) has a different form. Thus the subroutine that returns the potential gradients returns two sets of  $x$  derivatives and the appropriate one is used for the detailed reflection.

### A.5. Detailed reflection scheme

Stars in a close binary can heat each other, and this mutual heating leads to easily observed consequences. Wilson (1990) divides the “reflection” theory into four main parts: the geometric aspect, the bolometric energy exchange, the intensity from

an irradiated stellar atmosphere, and the effect on the envelope structure. In this paper Wilson gives a complete description of his “detailed reflection” scheme which treats the first two parts of the theory essentially exactly. We have fully implemented Wilson’s treatment of the reflection effect, which is a big improvement over the scheme used by Orosz & Bailyn (1997). There are two points about this scheme that are noteworthy:

(i) Wilson’s scheme makes use of *bolometric* limb darkening approximations. We have seen that the limb darkening in cool giants is not well parameterised by the common limb darkening laws. Fortunately, in most practical situations, a relatively hot star with a high surface gravity ( $\log g > 4$ ) irradiates a much cooler star. The irradiation of the hot star by the cool star can be neglected (in which case we don’t care about the details of the cool star limb darkening), and the well-known limb darkening laws apply nicely to the hot, high-gravity star.

(ii) Wilson introduced the use of the  $R$ -function in the reflection scheme to allow for multiple reflection. For each element, the  $R$ -function is defined by

$$R_1(x, y, z) = 1 + \frac{F'_2}{F_1(x, y, z)} \quad (\text{A.5})$$

$$R_2(x, y, z) = 1 + \frac{F'_1}{F_2(x, y, z)} \quad (\text{A.6})$$

where  $F'_2/F_1(x, y, z)$  is the ratio of the total irradiating flux from star 2 seen at the local surface element on star 1 and  $F'_1/F_2(x, y, z)$  is the reverse. The new temperatures of the irradiated surface elements are then

$$T_1^{\text{new}}(x, y, z) = T_1^{\text{old}}(x, y, z) R_1^{1/4}(x, y, z) \quad (\text{A.7})$$

$$T_2^{\text{new}}(x, y, z) = T_2^{\text{old}}(x, y, z) R_2^{1/4}(x, y, z). \quad (\text{A.8})$$

It is usually assumed that the specific intensity of an irradiated surface element is the same as the intensity of an unheated surface element with the same temperature. At some point the irradiation become intense enough that this assumption must break down. Alencar & Vaz (1999) have computed some irradiated atmosphere models and presented limb darkening coefficients for use in light curve synthesis codes. The use of these coefficients is perhaps somewhat limited as the widely available versions of the popular W-D code have only a single limb darkening law for the entire star (which of course includes the unheated back hemisphere). One of us (PHH) is in the process of computing irradiated atmospheres with the PHOENIX code. It should be relatively simple to include the irradiated atmospheres into the ELC code, at least for specific binaries. There exist many eclipsing close binaries where a hot subdwarf O/B star irradiates its G-M main sequence companion (e.g. Hilditch et al. 1996). Such systems can provide strong tests of irradiated atmospheres.

### A.6. Flared accretion disk

The accretion disk used in the Orosz & Bailyn (1997) code was a flattened cylinder. To make the disk perhaps more realistic, we have modified the disk so that its thickness as a function of the radius is proportional to the radius. The disk, if present,

is always around star 2. Star 2 does not necessarily have to be present (as in an X-ray binary). The disk is described by five basic parameters:  $r_{\text{outer}}$ , the radius of the outer edge of the disk in terms of the effective Roche lobe radius of star 2;  $r_{\text{inner}}$ , the inner radius of the disk in the same units as the filling factor of star 2 ( $f_2$ );  $\beta_{\text{rim}}$ , the opening angle of the disk rim above the plane;  $T_{\text{disk}}$ , the temperature of the *inner* disk (in the Orosz & Bailyn (1997) code the temperature of the *outer* rim was specified); and  $\xi$ , the power-law exponent on the temperature profile of the disk:

$$T(r) = T_{\text{disk}}(r/r_{\text{inner}})^\xi. \quad (\text{A.9})$$

For a steady-state accretion disk,  $\xi = -3/4$  (Pringle 1981). For a disk heated by a central source, the exponent  $\xi$  can take on a range of values ( $-3/4 \lesssim \xi \lesssim -1/2$  (e.g. Friedjung 1985; Vrtilik et al. 1990; Bell 1999)).

Since the surface of the disk is flared, each element on the face of the disk will have different “projection factors”  $\Gamma$  to the line of sight. Here  $\Gamma$  is equivalent to the angle  $\mu$  discussed above. We define a polar coordinate system centred at the centre of the disk. The angle  $\theta$  is measured from the  $x$ -axis in the direction of the positive  $y$ -axis. For a given the orbital phase  $\phi$ ,  $\Gamma(r, \theta)$  is given by

$$\begin{aligned} \Gamma(r, \theta) = & -\cos \phi \sin i \sin \beta \cos \theta \\ & -\sin \phi \sin i \sin \beta \sin \theta \\ & + \cos i \cos \beta. \end{aligned} \quad (\text{A.10})$$

If  $\Gamma(r, \theta) < 0$ , the point is not visible.

There are several geometrical details which we must account for when the disk is flared and/or when star 2 has a relatively large radius. First, for cases when the inclination  $i$  is within  $\beta$  degrees of 90, parts of the disk face that have  $\Gamma(r, \theta) > 0$  will be below the rim as seen by a distant observer. To account for these hidden points, we define the “horizon” of the top rim of the disk. In this discussion the horizon of an object is the outline of the object in sky coordinates. A point on the disk face is visible if its sky coordinates are *inside* the top horizon. Star 2 can block parts of the disk if its radius is relatively large. Since we currently require the inner radius of the disk to be equal to the radius of star 2 (if present), some or all of the “bottom” part of star 2 may be hidden by the disk. Again, the shadowing of the disk by star 2 and the lower part of star 2 by the disk is easily accounted for by defining the suitable horizons. Finally, a disk with a large radius can inhibit the mutual irradiation of the two stars since the “top” of star 1 cannot “see” the “bottom” of star 2, and vice-versa. If a disk is present then inside the detailed reflection subroutine each line of sight between points on star 1 and star 2 is checked to see if it passes through the disk.

Currently we assume that each surface element on the disk has a specific intensity that is the same as a normal stellar atmosphere. Following Pringle et al. (1986) we use the model with the largest gravity for each effective temperature. Of course, much more detailed model atmospheres specific to accretion disks are available (for example the grid of models for accretion disks in cataclysmic variables presented by Wade & Hubeny

1998), and in principle a separate intensity table for accretion disks can almost trivially be added to ELC. Indeed, Linnell & Hubeny (1996) create light curves for binaries with disks by first computing detailed spectra for the disk using the Hubeny codes. However, the Hubeny code TLUSDISK is best suited for atmospheres hotter than about 10,000 K, and as such cannot really be used to model the cool outer parts of many disks. As it is now, our treatment of the accretion disk is perhaps the most appropriate for systems where the disk is optically faint and its main effect on the light curves is geometrical (i.e. it eclipses the bright mass-losing star). Examples of such systems are W Crucis (Zola 1996), GRO J1655-40 (Orosz & Bailyn 1997), and BG Geminorum (Benson et al. 2000).

### A.7. Third light

In many Algol type binaries there is good evidence for a fainter third star that is gravitationally bound. For example, the  $O - C$  residuals of the eclipse timings of SW Lyncis are periodic and can be explained by the presence of a third body in a 5.8 year eccentric orbit about the inner binary (Ogloza et al. 1998). In such triple systems, the “third light” dilutes the observed amplitudes of the light curves from the binary, provided of course that the third star is sufficiently bright. We have a trivial way to self-consistently add third light to light curves in different bandpasses. In ELC, the user specifies three parameters for the third light: the temperature of the third star, its gravity, and its surface area relative to the surface area of star 1. The code interpolates the filter-integrated intensities for the third star from the table, scales appropriately based on the surface area ratio, and adds the light to each light curve.

### A.8. Accuracy of light curves through eclipse

The integration of the observed flux from a single star is straightforward and is sufficiently accurate for a reasonably small number of surface elements. However, quantisation errors can become noticeable in the light curve of a star going through an eclipse. In many cases (e.g. grazing eclipses, no reflection effect) the number of surface elements can be modestly increased so that a smooth light curve can be obtained without a large increase in the CPU time required to compute the model. In other cases (e.g. deep eclipses and several iterations of detailed reflection) the number of surface elements needed to get smooth light curves becomes so large that the required CPU time becomes excessive. Thus ELC has two features which prove to be quite effective in greatly reducing the numerical noise of light curves through eclipse.

### A.8.1. Improved horizon definition for the eclipsing star

The horizon of the eclipsing star (the one “in front”) is defined to be a collection of points on the star which have  $\mu = 0$ . In previous versions of the code, the program would step through the surface grid in the “ $\alpha$ ” direction and record which surface elements were last visible (i.e. the last point with  $\mu > 0$ ). The re-

sulting collection of sky coordinates of these surface elements would then define the horizon of the star. There is a systematic error introduced when the number of surface elements is small since the numerical horizon of the star will be slightly smaller than the actual horizon. In the current version of the code, the program steps along each latitude row and records the  $\phi$ -coordinate of the last visible point  $\phi_{\text{vis}}$  and the  $\phi$ -coordinate of the first point hidden below the horizon  $\phi_{\text{hid}}$ . A simple bisection procedure is used to find the  $\phi$ -coordinate (with a given latitude  $\theta_i$ ) where  $\mu = 0$ . Fifteen iterations of this bisection procedure are enough to find  $\phi_{\text{hor}}$  to better than  $10^{-5}$  radians when  $N_\beta = 6$  (i.e. 24 longitude points). The corresponding angles  $\mu$  are all  $\lesssim 5 \times 10^{-6}$ . The  $x$  and  $y$  sky coordinates of the point with the surface coordinates  $\theta_i, \phi_{\text{hid}}$  are then determined. A similar procedure is done where the program steps through the  $\theta$  angle for each longitude  $\phi_i$  and  $\theta_{\text{hor}}$  is found from  $\theta_{\text{vis}}$  and  $\theta_{\text{hid}}$  using bisection. After the list of points on the star with  $\mu = 0$  is generated, the  $x$  and  $y$  rectangular coordinates of each point on the sky are converted to a  $R, \Theta$  polar coordinate system and sorted in the polar angle  $\Theta$ . The sorted array forms a convex polygon on the sky. If the number of surface elements on the star is relatively small ( $N_\alpha \lesssim 30$  and  $N_\beta \lesssim 6$ ), then the actual horizon of the star can have some curvature between adjacent points on the polygon. Since the radius  $R$  as a function of  $\Theta$  is always a very smooth function, we use spline interpolation to resample  $R$  for every  $1^\circ$  in  $\Theta$ . The new resampled polygon with 360 points always has enough points so that the horizon of the star essentially has no curvature between adjacent points. We have done numerous tests and found that the horizons derived using a small number of surface elements with the new routine are always the same as the horizons found by the old routine with a very large number of surface elements ( $N_\alpha \approx 400$  and  $N_\beta \approx 100$ ).

#### A.82. Fractional surface elements on the eclipsed star

To compute the observed flux in a given bandpass from a star at a given phase, we numerically evaluate the integral in Eq. 9 using all of the surface elements with  $\mu > 0$ :

$$I_{\text{FILT}} = \sum_{i=1}^{N_\alpha} \sum_{j=1}^{4N_\beta} I_{\text{FILT}}(\mu_{i,j}) \mu_{i,j} r_{i,j}^2 \Delta\theta \Delta\phi / \cos \beta_{i,j} \quad (\text{A.11})$$

where  $\Delta\theta$  and  $\Delta\phi$  are the angular spacings of the elements in latitude and longitude, respectively, and where  $\beta$  is the angle between the surface normal and the radius from the centre of the star. In other words, we perform a simple numerical quadrature along each latitude row where the points are equally spaced in the angle  $\phi$ . If there is an eclipsing body in front of the star whose flux is being evaluated, then each point on the star in back is projected onto the sky and a simple routine is used to see if this point is inside the polygon representing the horizon of the body in front. If the point in question is eclipsed, its flux contribution is simply left out of the summation.

In general, the horizon of the star in front will not pass exactly between two adjacent points on a given latitude row on

the star in back. As a result there will be “visible” points that are actually centred in partially eclipsed surface elements and “eclipsed” points that are centred in partially visible surface elements. If the number of surface elements on the star in back is large enough, the contribution from the fractionally eclipsed surface elements will tend to cancel out. However, it is much more computationally efficient to use a smaller number of surface elements and make a correction for the fractionally eclipsed pixels. At each latitude row  $\theta_i$  on the star in back, the program determines the  $\phi$ -coordinate of the last point visible before the horizon of the eclipsing body  $\phi_{\text{vis}}$  and the  $\phi$ -coordinate of the first point hidden behind the horizon of the eclipsing body  $\phi_{\text{hid}}$ . Another bisection procedure is used to determine the  $\phi$ -coordinate on the star in back where the horizon of the eclipsing body intersects the  $\theta_i$  latitude row  $\phi_{\text{hor}}$ . If  $|\phi_{\text{hor}} - \phi_{\text{vis}}| < \Delta\phi/2$ , then the last point visible before the horizon is centred in a partially eclipsed surface element and a negative correction is added to the flux summation:

$$F_{\text{corr}} = \left[ \frac{2(\phi_{\text{hor}} - \phi_{\text{vis}}) - \Delta\phi}{\Delta\phi} \right] F_{\text{vis}} \quad (\text{A.12})$$

where  $F_{\text{vis}}$  is flux from the last visible point, i.e.

$$F_{\text{vis}} = I_{\text{FILT}}(\mu_{i,j}) \mu_{i,j} r_{i,j}^2 \Delta\theta \Delta\phi / \cos \beta_{i,j}. \quad (\text{A.13})$$

Likewise, if  $|\phi_{\text{hor}} - \phi_{\text{hid}}| < \Delta\phi/2$ , then the first point hidden behind the horizon is centred in a partially visible surface element and a positive correction is added to the flux summation:

$$F_{\text{corr}} = \left[ \frac{\Delta\phi - 2(\phi_{\text{hor}} - \phi_{\text{hid}})}{\Delta\phi} \right] F_{\text{hid}} \quad (\text{A.14})$$

where  $F_{\text{hid}}$  is the flux the eclipsed point. If there is an annular eclipse, then this procedure for finding  $\phi_{\text{hor}}$  may have to be done twice for a given latitude row. We have tested this simple interpolation procedure quite extensively and have found it to be quite effective. Smooth light curves through eclipse can be obtained for grid sizes as small as  $N_\alpha = 14$  and  $N_\beta = 6$ .

#### A.9. Comparison with Wilson and Devinney

We have done extensive testing of the ELC code in its black body mode against the W-D code. Unfortunately, there is some confusion over the notation of some of the input parameters between the two codes. In particular,  $\Omega$  in ELC is the ratio of the star’s angular velocity to the orbital velocity, whereas  $\Omega$  in W-D refers to the potential. The W-D  $\Omega$ -potentials essentially define the shapes of the stars. Perhaps to conserve parity,  $f$  in ELC is the “filling factor” which has the same function as the  $\Omega$ -potential in W-D (i.e. it defines the shape of the star), whereas in W-D,  $F$  is the ratio of the star’s angular velocity to the orbital velocity (ELC’s  $\Omega$ ). The phase convention between the two codes is different. In ELC, star 1 is in front of star 2 at phase 0.0, whereas in W-D star 1 is *behind* star 2 at phase 0.0.

To facilitate comparisons between ELC and W-D, we do two things. First, since the internal form of the potential is the same for both codes, ELC prints out the program values of the

potentials which then are the input  $\Omega$  potentials for W-D. Second, we add a phase shift of 0.5 to the W-D light curves (the ‘pshift’ input parameter). We computed various model binary light curves using the two codes and compared them by normalising the light curves at phase 0.25 (quadrature). We of course used exactly the same effective wavelengths, limb darkening laws and coefficients, and reflection schemes for both codes. In most cases, the light curves agreed to better than 0.1 per cent (better than 1 millimag). If we compared the light curves by adjusting the normalisation of one of the curves to match the other, then the largest deviations became even smaller.

ELC also computes radial velocity curves (Wilson & Sofia 1976). The velocity curves from ELC agree with the W-D velocity curves to better than 0.1 per cent.

Finally, we compared computed geometric quantities between the two codes (i.e. the ‘polar’ radius, ‘point’ radius, etc.). The agreement was essentially exact. We also computed sphere-equivalent Roche lobe radii and compared our results with Eggleton’s (1983) results and likewise found nearly exact agreement.

## References

- Alencar S.H.P., Vaz L.P.R., 1999, *A&AS* 135, 555  
 Al-Naimiy H.M., 1978, *Ap&SS* 53, 181  
 Avni Y., 1978, In: Giacconi R., Ruffini R. (eds.) *Physics and Astrophysics of Neutron Stars and Black Holes*. North-Holland, Amsterdam, p. 42  
 Avni Y., Bahcall J.N., 1975, *ApJ* 197, 675  
 Bailey J., 1975, *J. Brit. Astron. Assoc.* 85, 217  
 Belczyński K., Mikolajewska J., 1998, *MNRAS* 296, 77  
 Bell K.R., 1999, *ApJ* 526, 411  
 Bell R.A., Gustafsson B., 1989, *MNRAS* 236, 653  
 Benson P., Dullighan A., Bonanos A., McLeod K.K., Kenyon S.J., 2000, *AJ* 119, 890  
 Bessell M.S., 1990, *PASP* 102, 1181  
 Bessell M.S., Brett J.M., 1988, *PASP* 100, 1134  
 Callanan P.J., van Paradijs J., Rengelink R., 1995, *ApJ* 439, 928  
 Carbon D.F., Gingerich O.J., 1969, In: Gingerich O.J. (ed.) *Theory and Observations of Normal Stellar Atmospheres*. MIT Press, Cambridge (Mass.), p. 377  
 Claret A., 1998, *A&A* 335, 647  
 Díaz-Cordovés J., Giménez A., 1992, *A&A* 259, 227  
 Eaton J.A., Hall D.S., Honeycutt R.K., 1991, *ApJ* 376, 289  
 Eggleton P.P., 1983, *ApJ* 268, 368  
 Etzel P.B., Olson E.C., 1995, *AJ* 110, 1809  
 Faulkner J., Flannery B.P., Warner B., 1972, *ApJ* 175, L79  
 Fekel F.C., Joyce R.R., Hinkle K.H., Skrutskie M.F., 2000, *AJ* 119, 1375  
 Friedjung M., 1985, *A&A* 146, 366  
 Gray D.F., 1992, *Observations and Analysis of Stellar Photospheres*. Cambridge University Press, Cambridge  
 Haswell C.A., Robinson E.L., Horne K., Stiening R.F., Abbott T.M.C., 1993, *ApJ* 411, 802  
 Hauschildt P.H., Baron E., Allard F., 1997, *ApJ* 483, 390  
 Hauschildt P.H., Allard F., Ferguson J., Baron E., Alexander D.R., 1999, *ApJ* 525, 871  
 Heemskerk M.H.M., van Paradijs J., 1989, *A&A* 223, 154  
 Hilditch R.W., Harries T.J., Hill G., 1996, *MNRAS* 279, 1380  
 Hill G., Hutchings J.B., 1970, *ApJ* 162, 265  
 Hofmann K.-H., Scholz M., 1998, *A&A* 335, 637  
 Hric L., Petrik K., Urban Z., Niarchos P., Anupama G.C., 1998, *A&A* 339, 449  
 Hubeny I., 1988, *Comput. Phys. Comm.* 52, 103  
 Hubeny I., 1991, In: Bertout C., Collin S., Lasota J.-P., Tran Thanh Van J., (eds.) *Structure and Emission Properties of Accretion Disks*. Fong & Sons, Singapore, p. 227  
 Hubeny I., Lanz T., Jeffrey C.S., 1994, In: Jeffrey C.S. (ed.) *Newsletter on Analysis of Astronomical Spectra*. No. 20, St Andrews Univ., p. 30  
 Jørgensen U.G., Johnson H.R., Nordlund A., 1992, *A&A* 261, 263  
 Kenyon S.J., Garcia M.R., 1986, *AJ* 91, 125  
 Klingsmith D.A., Sobieski S., 1970, *AJ* 75, 175  
 Kneib L.B.G., Scarfe C.D., Mayor M., Baldwin B.W., Meatheringha S.J., 1986, *A&A* 168, 72  
 Kopal Z., 1959, *Close Binary Systems*. John Wiley & Sons, New York  
 Kraft R.P., 1958, *ApJ* 127, 620  
 Kruszewski A., Semeniuk I., 1999, *Acta Astron.* 49, 561  
 Kurucz R.L., 1979, *ApJS* 40, 1  
 Lacy C.H.S., Torres G., Claret A., et al., 2000, *ApJ* 119, 1389  
 Lines H.C., Lines R.D., McFaul T.G., 1988, *AJ* 95, 1505  
 Linnell A.P., 1984, *ApJS* 54, 17  
 Linnell A.P., Hubeny I., 1994, *ApJ* 434, 738  
 Linnell A.P., Hubeny I., 1996, *ApJ* 471, 958  
 Linnell A.P., Hubeny I., Harmanec P., 1998a, *ApJ* 509, 379  
 Linnell A.P., Etzel P.B., Hubeny I., Olson E.C., 1998b, *ApJ* 494, 773  
 Lucy L.B., 1967, *Z. f. Astroph.* 65, 89  
 Marsh T.R., Robinson E.L., Wood J.H., 1994, *MNRAS* 266 137  
 McClintock J.E., Remillard R.A., 1990, *ApJ* 350, 386  
 Milone E.F., Stagg C.R., Kurucz R.L., 1992, *ApJS* 79, 123  
 Mochejska B.J., Kaluzny J., Stanek K.Z., Krockenberger M., Sasselov D.D., 1998, *AJ* 118, 2211  
 Mochnacki S.W., Doughty N.A., 1972, *MNRAS* 156, 51  
 Ogloza W., Zola S., Tremko J., Kreiner J.M., 1998, *A&A* 340, 81  
 Olson E.C., 1993, *AJ* 106, 754  
 Olson E.C., Etzel P.B., 1993a, *AJ* 106, 759  
 Olson E.C., Etzel P.B., 1993b, *AJ* 106, 1162  
 Olson E.C., Etzel P.B., 1994, *AJ* 108, 262  
 Orosz J.A., Bailyn C.D., 1997, *ApJ* 477, 876 (Erratum *ApJ* 482, 1086)  
 Plez B., Brett J.M., Nordlund A., 1992, *A&A* 256, 551  
 Pols O.R., Tout C.A., Schröder K.-P., Eggleton P.P., Manners J., 1997, *MNRAS* 289, 869  
 Popper D.M., 1977, *PASP* 89, 315  
 Pringle J.E., 1981, *ARA&A* 19, 137  
 Pringle J.E., Verbunt F., Wade R.A., 1986, *MNRAS* 221, 169  
 Ribas I., Guinan E.F., Fitzpatrick E.L., et al., 2000, *ApJ* 528, 692  
 Sanwal D., Robinson E.L., Zhang E.-H., et al., 1996, *ApJ* 460, 437  
 Scholz M., Takeda Y., 1987, *A&A* 186, 200  
 Scholz M., Tsuji T., 1984, *A&A* 130, 11  
 Schröder K.-P., Pols O.R., Eggleton P.P., 1997, *MNRAS* 285 696  
 Selvelli P.L., Cassatella A., Gilmozzi R., 1992, *ApJ* 393, 289  
 Shahbaz T., 1998, *MNRAS* 298, 153  
 Shahbaz T., Ringwald F.A., Bunn J.C., et al., 1994, *MNRAS* 271, L10  
 Shahbaz T., Somers M., Yudin B., Naylor T., 1997, *MNRAS* 288, 1027  
 Tjemkes S.A., Zuiderwijk E.J., van Paradijs J., 1986, *A&A* 154, 77  
 van der Hooft F., Heemskerk M.H.M., Alberts F., van Paradijs J., 1998, *A&A* 329, 538  
 Van Hamme W., 1993, *AJ* 106, 2096  
 Van Hamme W., Wilson R.E., 1990, *AJ* 100, 1981  
 Van Hamme W., Wilson R.E., 1994, *BAAS* 185, 85.14

- Vrtilek S., Raymond J.C., Garcia M.R., et al., 1990, A&A 235, 162  
von Zeipel H., 1924, MNRAS 84, 665  
Wade R.A., Rucinski S.M., 1985, A&AS 60, 471  
Wade R.A., Horne K., 1988, ApJ 324, 411  
Wade R.A., Hubeny I., 1998, ApJ 509, 350  
Wilson R.E., 1979, ApJ 234, 1054  
Wilson R.E., 1990, ApJ 356, 613  
Wilson R.E., 1994, PASP 106, 921  
Wilson R.E., 2000, private communication  
Wilson R.E., Devinney E.J., 1971, ApJ 166, 605  
Wilson R.E., Sofia S., 1976, ApJ 203, 182  
Yudin B., Munari U., 1993, A&A 270, 165  
Zhang E.H., Robinson E.L., Nather R.E., 1986, ApJ 305, 740  
Zola S., 1996, A&A 308, 785  
Zola S., Hall D.S., Henry G.W., 1994, A&A 285, 531